

# Laser Texturing of Plasma Electrolytically Oxidized Aluminum 6061 Surfaces for Improved Hydrophobicity

**B. S. Yilbas**

Mechanical Engineering Department,  
King Fahd University of Petroleum & Minerals,  
Dhahran 31261, Saudi Arabia  
e-mail: bsyilbas@kfupm.edu.sa

**A. Matthews**

Department of Materials Science and Engineering,  
University of Sheffield,  
Sheffield S10 2TN, UK  
e-mail: a.matthews@sheffield.ac.uk

**C. Karatas**

Engineering College,  
Hacettepe University,  
Ankara, Turkey  
e-mail: doc\_cihan@hotmail.com

**A. Leyland**

Department of Materials Science and Engineering,  
University of Sheffield,  
Sheffield S10 2TN, UK

**M. Khaled**

Chemistry Department,  
King Fahd University of Petroleum & Minerals,  
Dhahran 31261, Saudi Arabia  
e-mail: mkhaled@kfupm.edu.sa

**N. Abu-Dheir**

Mechanical Engineering Department,  
King Fahd University of Petroleum & Minerals,  
Dhahran 31261, Saudi Arabia

**N. Al-Aqeeli**

Mechanical Engineering Department,  
King Fahd University of Petroleum & Minerals,  
Dhahran 31261, Saudi Arabia

**X. Nie**

Mechanical, Automotive and Materials Engineering,  
University of Windsor,  
Windsor, ON N9B 3P4, Canada  
e-mail: xnie@uwindsor.ca

*Laser surface texturing of plasma electrolytically oxidized aluminum 6061 alloy has been carried out through a controlled surface ablation under a high pressure nitrogen gas assistance. Morphological and metallurgical changes in the laser-treated region were examined using optical, scanning electron, and atomic force*

*microscopy, energy dispersive X-ray spectroscopy, and X-ray diffraction phase analysis. The hydrophobicity of the textured surface was assessed through water droplet contact angle measurements. It was found that a dense layer with a nanotexture/microtexture is developed at the surface after the laser treatment process. The assessment of the surface characteristics reveals that a superhydrophobic surface results from the laser treatment process; in which case, high water droplet contact angles are measured over the treated surface, which can be explained by known models of texture-induced superhydrophobicity.*  
[DOI: 10.1115/1.4027977]

## Introduction

Aluminum 6061 is a precipitation hardening aluminum–magnesium–silica alloy which is commonly used for aircraft structures [1], automotive parts [2], and food industry machinery [3]. The tribological properties of aluminum alloys can be improved by forming an oxide layer at the surface utilizing plasma electrolytic oxidation (PEO) [4], which is an advanced form of anodic oxidation incorporating a plasma discharge process [5]. The PEO process, when applied to an aluminum alloy workpiece, results in aluminum oxide layer formation at the surface, improving hydrophobicity [6]. Although surface hydrophobicity of the aluminum alloy can be improved through surface oxidation, its applications become limited compared to the “super hydrophobicity” characteristics demonstrated by other surfaces. Super hydrophobicity is of increasing interest for several applications including MEMS devices; however, the development and retention of properties are challenging and, in some cases, treated surfaces are prone to degradation when they are in contact with liquids for extended periods [7]. Nanotexturing/microtexturing of the geometric orientation and size of the surface features can enable super hydrophobicity at the textured surface, whilst retaining the wear and corrosion protective properties of the oxide film. Several surface texturing methods have been introduced; however, most of them are expensive and involve multiple processes or harsh conditions and specialized reagents [8–14]. Surface texturing methods previously investigated include phase separation [8], electrochemical deposition [9], plasma treatment [11], sol–gel processing [12], electrospinning [13], solution immersion [14], and laser-controlled surface ablation, the last of which may offer opportunities for cost effective texturing [6]. Gas-assisted laser nanotexturing/microtexturing of surfaces has several advantages over other methods [6,15,16] because it achieves a controlled ablation at the surface. In addition, the laser texturing process does not involve mechanical contact. Gas-assisted laser surface texturing of aluminum alloys incorporating high-pressure nitrogen gas causes formation of nitride species at the treated surface, which in turn further enhances the surface hydrophobicity by altering the surface energy [6]. Although laser ablation of surfaces has many advantages, excessive stress fields can be developed in the region of the treated surface because of the high temperature gradients formed during the process. This, in turn, can initiate thermally induced crack formation at the treated surface. Consequently, investigation into laser ablation of plasma electrolytically oxidized aluminum 6061 alloy surfaces becomes essential in relation to nanotexturing/microtexturing for improved hydrophobicity.

**Background and Literature Review.** Several research studies have been carried out to examine laser treatment of aluminum alloys. Surface characteristics of aluminum 6061-T6 alloy after an Nd:YAG pulsed-laser treatment were studied by Choi et al. [17]. They indicated that laser treatment modifies the surface morphology considerably. The diameter of the melted zone increased with surface roughness due to multiple reflection and absorption of the laser beam. Laser sintering of ultrananocrystalline diamond powders on aluminum 6061 T-91 alloy was carried out by Nair et al. [18]. They indicated that laser sintering to produce thick

Contributed by the Manufacturing Engineering Division of ASME for publication in the JOURNAL OF MANUFACTURING SCIENCE AND ENGINEERING. Manuscript received December 30, 2013; final manuscript received June 21, 2014; published online August 6, 2014. Assoc. Editor: Y. B. Guo.

diamond-like coatings with outstanding mechanical and tribological properties and excellent bonding was possible and the sintering offered the means to produce an extremely lightweight, strong, and wear-resistant material. The microstructure and mechanical properties of aluminum 6061 alloy after laser treatment were investigated by Xu et al. [19]. Their findings revealed that a large quantity of dispersed age-strengthening particles were precipitated during the laser treatment process, which in turn resulted in improved microhardness. The fatigue performance of aluminum 6061-T6 alloy subjected to a laser peening treatment was examined by Wang et al. [20]. They demonstrated that laser shock processing could effectively inhibit crack growth and, as a consequence, fatigue life was extended. Laser processing of aluminum 6061-T6 alloy and the mechanical properties of the resulting surface were investigated by Gencalp et al. [21]. They showed that the surface microhardness and tensile strength of the workpiece increased considerably after the laser treatment process. The influence of temporal variations in laser pulse shape on cracking susceptibility of aluminum 6061-T6 alloy was studied by Zhang et al. [22]. They indicated that use of a trailing ramp-down pulse shape affected the solidification morphology together with the width of the initial planar grain growth layer at the fusion boundaries; the dendrite and cell spacing increased with decreasing ramp-down gradient. Laser-assisted TiC coating on aluminum 6061 alloy and the wear characteristics of the surface were studied by Katipelli et al. [23]. They demonstrated that the wear resistance of the coated surface was higher than that of an untreated surface. Laser treatment of aluminum 6061-T6 alloy surface and residual stress formation were studied by Gomez-Rosas et al. [24]. They demonstrated that the residual stress was compressive in-plane at the surface and its magnitude was less than the yield stress of the substrate material. Laser treatment of aluminum 6061-T6 alloy surface and wear characteristics of the resulting surface were examined by Sanchez-Santana et al. [25]. They observed that the wear rate decreased as the pulse density increased at the workpiece surface. The precipitation hardening of aluminum 6061-T6 alloy using a low energy laser beam was studied by Sathyajith and Kalainathan [26]. They showed that the case depth of the laser-treated layer extended over a considerable volume below the surface, which was validated by the microhardness data. Surface characterization of DC PEO of the aluminum alloy was presented by Khan et al. [27]. They provided the correlations between internal stress and coating thickness. In addition, they suggested that specific PEO treatment regimes could be used to produce thick coatings with low stress levels. Impedance spectroscopy characterization of the PEO process (and resulting PEO coatings on aluminum) was performed by Parfenov et al. [28]. They demonstrated that the approaches introduced allowed appraisal of frequency response of PEO microdischarges to assess the optimal frequency for pulsed bipolar PEO. Plasma electrolytic nitrocarburizing of stainless steel surface was investigated by Nie and co-workers [29]. They indicated that the electrochemical properties of the treated layers were closely related to the microstructure and composition, which could be improved through a plasma electrolytic nitrocarburizing process. Electrochemical characteristics of laser-treated alumina surface were studied by Yilbas et al. [30]. The findings revealed that electrochemical properties of the surface, as measured by the corrosion rate, improved significantly after the laser treatment process. Morphological and metallurgical characteristics of laser-treated alumina tiles with the presence of hard particles were studied by Yilbas et al. [31,32]. They showed that laser-treated surfaces were free from large size asperities and a dense layer formed at the surface improved microhardness at the surface of the treated layer.

Although separate studies into PEO and laser microtexturing/nanotexturing of alumina alloy surfaces have previously been carried out [27–31], texturing of the surface for super-hydrophobicity and wear testing of the resulting surface were not studied. The PEO process produces an alumina layer at the surface of aluminum alloy. However, the surface characteristics including surface

energy and texture of the resulting alumina surface do not yield hydrophobic characteristics. In addition, delamination of the oxide layer and asperities formed at the surface, due to local high current intensity [27], can limit the practical application of the surface when the hydrophobicity is required. Therefore, the present study investigates the surface characteristics of laser-textured plasma electrolytic oxidized aluminum 6061 alloy in relation to surface hydrophobicity. Laser-controlled ablation of the treated surface was carried out under high nitrogen gas pressure to generate micropile/nanopile at the surface, which promotes super hydrophobicity properties. The laser power intensity distribution at the workpiece surface is Gaussian and peak power intensity occurs at the centre of the irradiated spot. The ablation takes place in the region close to the irradiated spot center and melting occurs in the vicinity of the irradiated spot edge. Laser scanning takes place through repetitive pulsation at the surface. Consequently, melt flow from the irradiated spot edge modifies the cavity shape and size at the irradiated surface due to the repetitive pulse irradiations and scanning of the workpiece during the ablation process. Morphological and metallurgical changes are examined in the laser-treated layer using optical, electron scanning, and atomic force microscopy, energy dispersive X-ray spectroscopy, and X-ray diffraction analysis. Water droplet contact angles are measured for the laser treated and untreated surfaces to assess the hydrophobic state of the treated surface.

## Experimental Equipment and Procedure

Aluminum 6061 alloy samples 25 mm diameter and 5 mm thick were used. The surface of the alloy was plasma electrolytically oxidized prior to the laser treatment process. The electrolytic oxidation process was carried out under DC polarization and the electrolyte temperature was kept below 40 °C during the process. The parameters incorporated in the PEO process are given in Table 1. A CO<sub>2</sub> laser (LC-ALPHAIII) delivering an output power of 2 kW was used to irradiate the workpiece surface; the focal length of the focusing lens was 127 mm. The laser beam diameter focused at the workpiece surface was ~0.25 mm. Nitrogen assisting gas emerging from the conical nozzle and co-axially with the laser beam was used. In the light of the previous study [6], laser treatment tests were repeated several times, incorporating different laser parameters, resulting in the selection of parameters which generate minimum surface defects, such as very small cavities—with no cracks (or crack networks). Increasing the laser power at the workpiece by 10%, while keeping the laser scanning speed constant, caused cavity formation at the surface, which in turn increased the surface roughness considerably and lowered the contact angle of the water droplet. However, similar behavior was also observed when the laser scanning speed was reduced by 10% while keeping the laser output power constant. On the other hand, increasing the laser scanning speed or lowering laser output power did not result in a nanopillar texture, which gives rise to high contact angles. (Table 1 gives the contact angle measurements for various laser treatment parameters.) Laser treatment conditions are given in Table 2.

Material characterization of the laser-treated surfaces was carried out using optical microscopy, SEM, AFM, energy dispersive spectroscopy (EDAX), and XRD. A Jeol 6460 electron microscope was used for SEM examinations and a Bruker D8 advance diffractometer is used for XRD analysis (CuK $\alpha$  radiation  $\lambda =$  with

**Table 1 Contact angles measured for various laser output power levels**

Fluence (J/cm <sup>2</sup> )	Contact angle (deg)
$1.21 \times 10^4$	93.2 ( $\pm 5$ )
$1.34 \times 10^4$	151.6 ( $\pm 5$ )
$1.47 \times 10^4$	112.4 ( $\pm 5$ )

**Table 2 Parameters used during PEO process**

Electrolyte solution	Treatment time (min)	Current (A)	Final voltage (V)	Surface roughness	
				Before treatment (mm)	After treatment (mm)
8 g/l silicate + 4 g/l tungstate	5	2	488	0.18	1.33

0.154 nm). The typical setting of the XRD instrument was 40 kV and 30 mA and scanning angle ( $2\theta$ ) in the range of 20 deg–90 deg. Surface roughness measurement of the laser-melted surfaces was performed using an Agilent 5100 AFM/SPM in contact mode. The tip was made of silicon nitride probes ( $r = 20\text{--}60$  nm) with a manufacturer specified force constant,  $k$ , of 0.12 N/m.

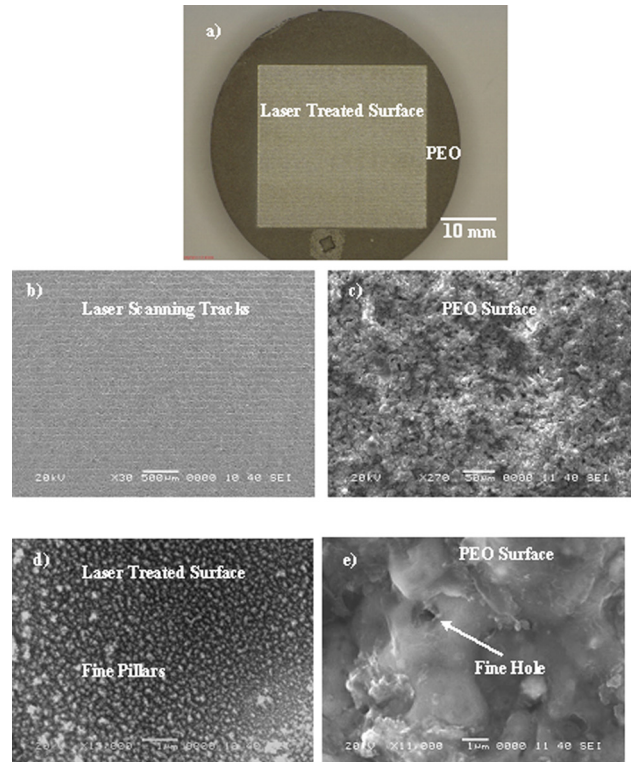
A microphotronics digital hardness tester (MP-100TC) was used to obtain Vickers micro-indentation hardness values at the surface of the nitride layer. The standard test method for Vickers indentation hardness of advanced ceramics (ASTM C1327-99) was adopted. Microhardness was measured at the workpiece surface after the laser treatment process. The measurements were repeated five times at each location for the consistency of the results.

A linear microscratch tester (MCTX-S/N: 01-04300 [9]) was used to determine the friction coefficient of the laser treated and untreated surfaces. The equipment was set at the contact load of 0.03 N and end load of 5 N. The scanning speed was 5 mm/min and loading rate was 5 N/min. The total length for the scratch tests was 5 mm.

The wetting experiment was performed using a Kyowa (model—DM 501) contact angle goniometer. A static sessile drop method was employed for the contact angle measurement. The contact angle between the droplet and the heat treated surface was measured using de-ionized water as the droplet medium. Droplet volume was controlled by an automatic dispensing system having a volume step resolution of 0.1  $\mu$ l. Still images were captured, and contact angle measurements were performed after 1 s of deposition of water droplet on the surface.

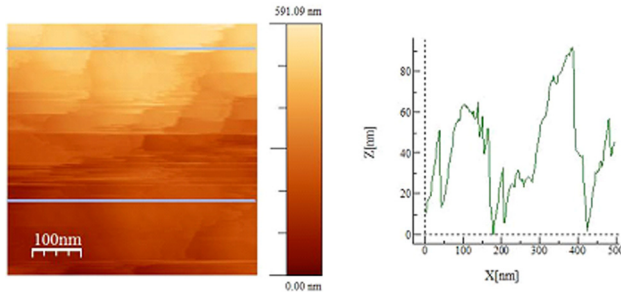
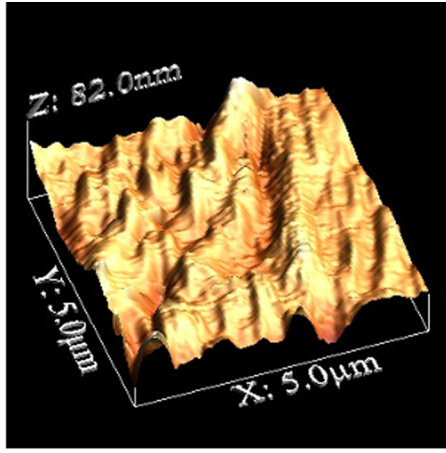
## Results and Discussion

Figure 1 shows optical photograph (Fig. 1(a)) and SEM images of the laser modified (Figs. 1(b) and 1(d)) (and unmodified) PEO-treated surface (Figs. 1(c) and 1(e)). The unmodified PEO surface is free from large cracks and voids; however, a porous morphology can be observed at the surface, which is common for the PEO processing. Pore diameter is influenced by the plasma current density during the PEO process [27,32] and the porous morphology contributes significantly to surface roughness of the workpiece, the Ra value of which is in the order of 0.9  $\mu$ m. The pores size varies from 0.1  $\mu$ m to 4.5  $\mu$ m and their presence contributes to enhancement of absorption of the laser irradiation at the surface, through multiple, internal reflection within the pores. Since the surface reflectivity of the aluminum alloy is high (82%), for the wavelength of employed laser irradiation, [33–35], the presence of porosity increases the energy transfer efficiency due to internal reflection of the incident laser beam in the pores during processing. After laser modification, the PEO-treated surface is free from cracks and large asperities including voids, cavities, and large size pores. Regular laser scanning tracks (which result from continuous scanning overlapping of the laser spots) are visible at the surface. It should be noted that the laser beam irradiates the surface at high frequency (1500 Hz) during the laser processing, which in turn results in an overlap ratio of over 70% for the irradiated spots along each laser scanning track. Since the laser power input at the surface Gaussian, the peak power intensity occurs at the irradiated spot center follows a distribution. Consequently, through proper selection of the laser intensity, the cavity size and depth can be controlled precisely at the irradiated surface during the ablation process—and thus a desired surface texture can be produced as a



**Fig. 1 Optical and SEM micrographs of plasma electrolytically oxidized PEO and after the laser treatment of PEO surfaces: (a) optical photograph showing laser treated and PEO surface, (b) laser-treated PEO surface, (c) PEO surface, (d) close view of laser treated PEO surface, and (e) close view of PEO surface**

consequence of the ablation process regime applied. However, the local temperature exceeds the melting temperature of the substrate material in the vicinity of the irradiated spot, causing molten flow into the cavity after its formation. This situation is particularly observed across two successive irradiated spots during the laser scanning of the surface. In this case, the molten material within the most recently formed spot flows (and slightly fills) the previously formed cavity in a neighboring location. This modifies the resulting texture along the laser scanning tracks; consequently, the texture pattern formed differs along the laser scanning tracks. However, this variation changes the pillar height slightly, within the texture. The variation of surface texture can also be seen from Fig. 2, in which an AFM image and a surface roughness plot are shown. It can be observed that the measured surface roughness is of the order of 400 nm and pillar heights are not noted from the surface roughness graph; consequently, this results in regular texture patterns, which are formed at the laser-treated surface. Moreover, the molten flows in between the laser scanning tracks are not observed. This indicates that excessive melting at the surface is avoided during the laser heating process can be correlated to consequent high quench rates at the surface. In this regard, high pressure nitrogen gas assistance contributes significantly to the enhancement of cooling rates at the surface. Although the surface cooling rate is high, no cracks or crack network is observed.



**Fig. 2** AFM images of laser-treated PEO surfaces: (a) 3D view of laser textured surface and (b) surface roughness

This is attributed to the self-annealing effect of recently formed laser scanning tracks adjacent to the previously formed tracks. Conduction heat transfer from the former to the latter modifies the cooling rates in the surface region while lowering thermally induced.

Figure 3 shows SEM micrographs of cross sections of laser modified (Figs. 3(a), 3(c), 3(e), and 3(f)) and unmodified regions (Figs. 3(b) and 3(d)). The unmodified sample corresponds to the plasma electrolytically oxidized workpiece. The oxidized region extends almost uniformly about  $10\ \mu\text{m}$  below the surface, which indicates the homogenous growth of oxides taking place during the PEO process. However, three regions can be identifiable across the cross section of the unmodified PEO-treated workpiece. A wide range of pores is observed in the first region, which is associated with the PEO treatment parameters and the electrolyte composition. In this case, a highly concentrated solution results in a thick porous layer in the surface region [27]. The second region consists of the condensed structures and appears below the porous region. The third region is a thin layer, situated in the interface between the oxide layer and the untreated substrate material. Moreover, delamination of the thin porous layer in the surface region of the oxide film is observed, which contributes to the surface roughness enhancement. In the case of the laser-modified workpiece cross section, the modified layer extends almost  $20\ \mu\text{m}$  below the surface and, based on the microstructure; it consists of three distinguishable regions. The first region is composed of a dense layer, formed of fine grains. Although the fine grains result in volume shrinkage in the surface region, no microcracks are observed. The overlapping of the irradiated spots (Fig. 3(a)), due to the high frequency (1500 Hz) laser pulse repetition, lowers the cooling rates in the surface region and suppresses thermally induced crack formation in this region. Consequently, recently formed irradiated spots act as heat sources and modify the cooling rates in the surface region during the pulse repetitions. An SEM micrograph of a cross section of the treated layer (normal to the laser scanning direction) is also shown in Fig. 3(a). The overlapping of the laser irradiated spots (and the depth of the heated region due to each spot) is visible in this micrograph. It should be

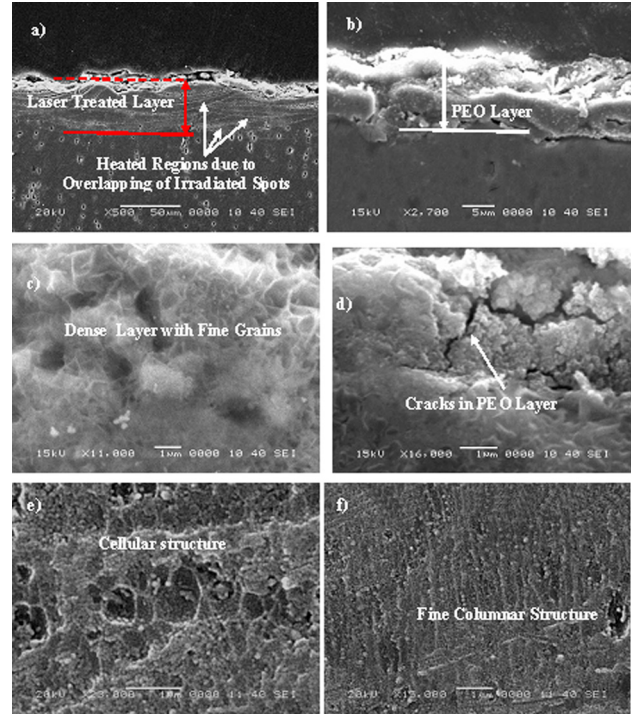


**Fig. 3** SEM micrographs of cross section of laser-treated and PEO layers: (a) laser-treated layer and heated regions due to overlapping of laser irradiated spots, (b) PEO layer, (c) dense layer with fine grains in laser treated layer, (d) cracks in PEO laser, (e) fine cellular structure in laser treated layer, and (f) fine columnar structure in laser treated layer

noted that the 1500 Hz laser pulse frequency results in irregular overlapping patterns of the heated region. In addition, the porous structures, as observed at the surface prior to the laser modification, are replaced with the dense structure in the surface region. Close examination of the SEM micrographs reveals that a columnar structure is formed beneath the dense layer and that, although the width of the columns is small, it increases with increasing depth below the surface. A demarcation line is clearly observed between the laser modified zone and the untreated base material. However, no clear heat affected zone is seen below the demarcation line, which may be attributable to the low thermal diffusivity of aluminum oxide.

Figure 4 shows an X-ray diffractogram for laser-treated plasma electrolytic oxidized and PEO surfaces. It can be observed from the X-ray diffractogram that  $\alpha\text{-Al}_2\text{O}_3$  is a major phase of the PEO

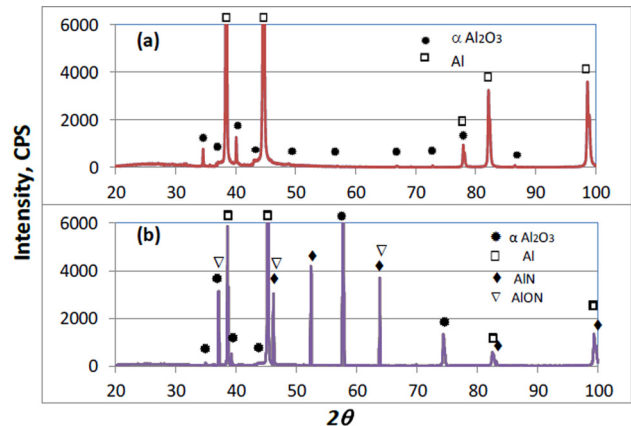


**Fig. 4** X-ray diffractogram for the laser treated PEO and PEO surfaces. AlON has the composition of  $\text{Al}_{2.85}\text{O}_{3.45}\text{N}_{0.56}$ .

**Table 3 Laser ablation conditions used in the experiment**

Scanning speed (cm/s)	Peak power (W)	Frequency (Hz)	Fluence (J/cm <sup>2</sup> )	Pulse duration (ms)	Nozzle gap (mm)	Nozzle diameter (mm)	Focus setting (mm)	N <sub>2</sub> pressure (kPa)
10	2000	1500	1.34 × 10 <sup>4</sup>	0.33	1.5	1.5	127	550

coating, Fig. 4(a). Al peaks with high intensity also appeared in the XRD pattern, indicating that the PEO coating was relatively thin and as a result the Al substrate was detected. The intensity of Al peaks for the PEO coating case was suppressed after laser modification, suggesting that laser processing increased the overall thickness of the modified surface region. The peak patterns changed significantly between 45 deg and 80 deg (2θ) which was caused by formation of new phases AlN and AlON. AlN peaks of (200), (102), (220), and (222) lattice planes at 2θ angles of 45.14 deg, 52.4 deg, 63.83 deg, and 82.73 deg, respectively, as well as AlON peaks of (311), (400), and (440) correspondingly at 2θ angles of 37.14 deg, 46.16 deg, and 63.83 deg are evident in Fig. 4(b). AlN can be formed through a two-step reaction. In this case, the first reaction is: Al<sub>2</sub>O<sub>3</sub> + 2C → Al<sub>2</sub>O + 2CO, which results in the formation of an aluminum monoxide [36] and the high pressure nitrogen gas assistance initiates the reaction Al<sub>2</sub>O + CO + N<sub>2</sub> → 2AlN + CO<sub>2</sub> in the second step [36]. The carbon dioxide formed releases from the irradiated surface during this process. However, the formation AlON at the surface is possibly explained in terms of high temperature chemical reactions; in which case, when the surface temperature reaches the melting temperature of alumina, single aluminum oxide is formed in the surface region through the following reaction: 2Al<sub>2</sub>O<sub>3</sub> → 4AlO + O<sub>2</sub>. The oxygen atom remains in the alumina structure and the presence of N<sub>2</sub> initiates the following reaction to form the AlON phase: 2AlO + N<sub>2</sub> → 2AlON [37]. The EDX data are given in Table 3 at two locations on the laser modified and unmodified surfaces. It is evident that the elemental composition of laser modified and unmodified PEO surfaces remain uniform in the surface region. The precise quantification of light elements, such as nitrogen, is difficult in EDX analysis; however, the presence of a significant nitrogen peak in the EDX spectral data indicates likely formation of nitride species at the laser treated surface. Microhardness data are given in Table 4 for laser modified, unmodified PEO-treated, and aluminum 6061 alloy surfaces. The microhardness increases significantly at the surface after laser processing of PEO, and is considerably higher than the base material (aluminum 6061 alloy) hardness. Moreover, the microhardness of the laser-modified surface is higher than that of the corresponding oxidized surface. The increase in the surface microhardness is associated with the formation of a dense layer, due to localized remelting and densification at the high cooling rates, where dense oxides and AlN phase were formed at the surface after the laser treatment—plus AlON process [38]. It should be noted that more work needs to be done in the future, in terms of formation and analysis of phase microstructural evolutions induced by the laser surface modification.

Figures 5 and 6 show friction coefficients of the PEO-treated laser modified surfaces and the resulting wear scar after scratch

**Table 4 Elemental composition of laser treated and untreated PEO surfaces obtained from EDS data (wt.%). Spectrum corresponds to a location at the surface and EDS data represent weight percentile of constituting elements.**

Spectrum	N	Mg	O	Al
Laser-treated PEO location 1	7.1	0.4	37.2	Balance
Laser-treated PEO location 2	6.8	0.3	39.4	Balance
PEO location 1	0	0.5	38.2	Balance
PEO location 2	0	0.5	40.5	Balance

testing. Laser treatment lowers the friction force, which can be attributed to reduced surface roughness and enhancement of surface microhardness after the laser modification process. The scar depth is much shallower for the laser processed PEO surface compared to that of the untreated PEO surface (Fig. 6(a)). Close examination of the micrographs reveals that the scar size is almost uniform (Fig. 6(b)). It should be noted that the scar length extends to 5 mm; however, only a small portion is shown in the micrograph for comparison purposes. The shallow scar depth is due to the increased hardness of the surface. In addition, no cracking around the scar mark is observed. Consequently, the surface fracture toughness reduction due to surface hardness enhancement is not significant. When comparing the wear scars at the surface due to laser and PEO treatments, the scar depth is slightly larger for the PEO treated surface than that of the laser modified surface. This indicates that the laser processing technique improves significantly microstructural integration in the surface region of the PEO-treated surface. It should be noted that laser-modified surfaces are pre-prepared through PEO treatment prior to laser treatment.

Figure 7 shows the photographs of droplets for the contact angle measurement on the laser modified and unmodified PEO surfaces. One of the parameters for the assessment of the wettability of solid surfaces is the contact angle which, on a perfectly smooth and chemically homogenous solid surface, is formulated by Young's equation [39]

$$\cos \theta = \frac{(\gamma_{sv} - \gamma_{sl})}{\gamma_{lv}} \quad (1)$$

where θ is the contact angle, γ<sub>sv</sub> is the interfacial tension of solid–vapor, γ<sub>sl</sub> is the interfacial tension of solid–liquid, and γ<sub>lv</sub> is the interfacial tension of liquid–vapor. However, Young's equation is limited to extremely smooth and homogenous surfaces. The formulation of the contact angle including surface roughness effects should therefore be considered [40,41]

$$\cos \theta_w = \frac{r(\gamma_{sv} - \gamma_{sl})}{\gamma_{lv}} \quad (2)$$

where θ<sub>w</sub> is the rough surface contact angle, r is the surface roughness factor, which is defined as the ratio between the actual and projected surface areas, i.e., r = 1 describes a perfectly smooth surface, and r > 1 represents the degree of roughening. The liquid surface interface consists of a liquid–solid and liquid–vapor interfaces; therefore, the contact angle should include contributions of the two-interfaces. The equation for the contact angle yields [41]

$$\cos \theta_c = f_1 \cos \theta_1 + f_2 \cos \theta_2 \quad (3)$$

where θ<sub>c</sub> is the apparent contact angle, f<sub>1</sub> is the surface fraction of liquid–solid interface, f<sub>2</sub> is the surface fraction of liquid–vapor interface, θ<sub>1</sub> is the contact angle for liquid–solid interface, and θ<sub>2</sub> is the contact angle for liquid–vapor interface. However, for the air–liquid interface, f<sub>1</sub> can be represented as f, which is the solid fraction, and the air fraction (f<sub>2</sub>) becomes (1 – f). The parameter f ranges from 0 to 1; in which case, f = 0 is where the liquid droplet is not in contact with the surface and f = 1 is where the surface is completely wetted. It was reported that in the Cassie–Baxter state [41], the small contact area between the liquid droplet and solid surface allowed the droplet to roll easily at the surface [42]. In

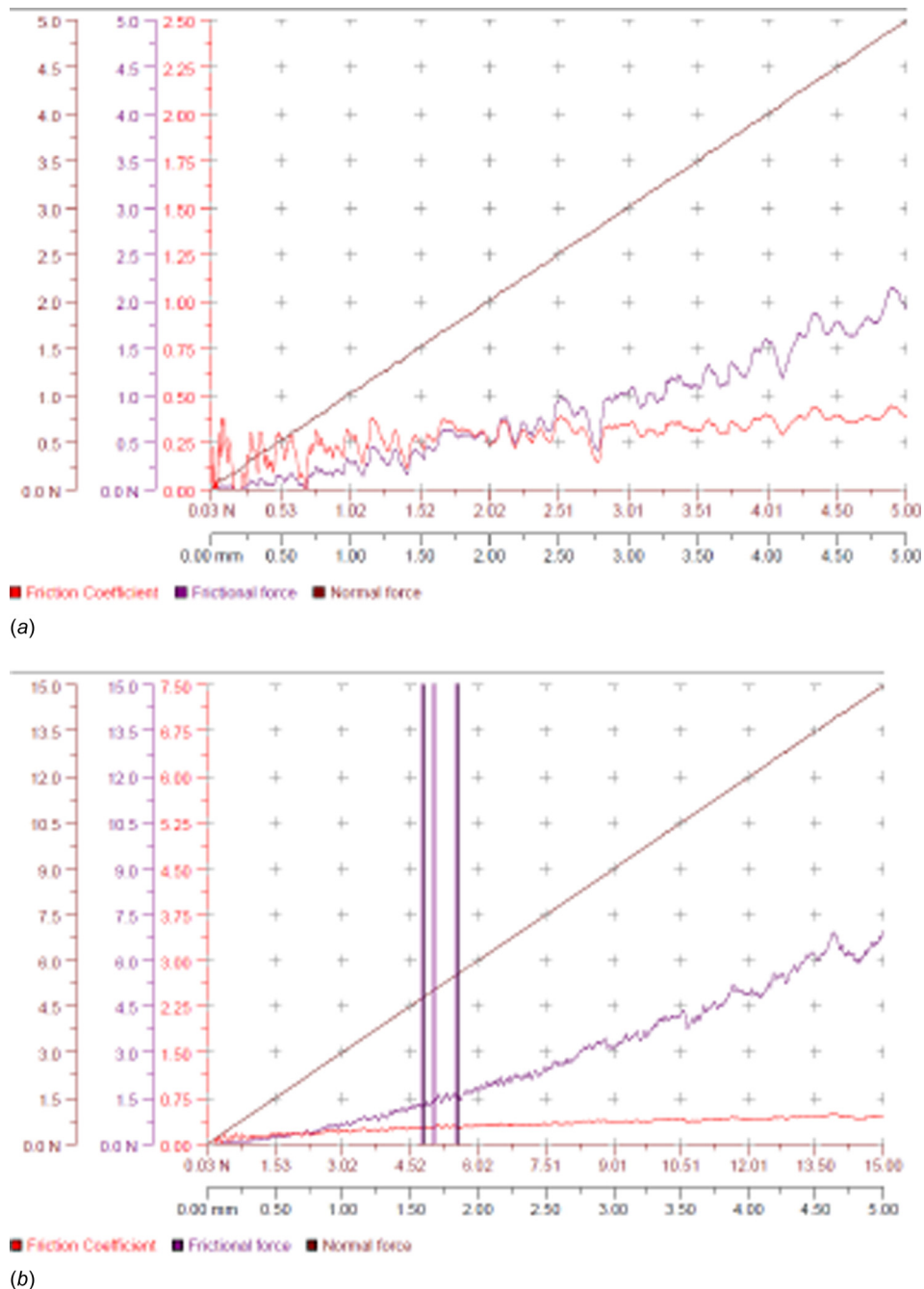


**Fig. 5 Scratch tests results for laser treated PEO surface and PEO surface. (a) Laser treated surface and (b) PEO treated surface.**

practice, the contact mode changes from the Cassie–Baxter state to the Wenzel state [40], when the surface texture changes or when the droplets impact at the surface [43], both states can co-exist on a nanopillared surface such as that developed in the present work [44]. However, when a liquid–air interface remains pinned at the pillars tops, a transition to the Wenzel state is possible, if the sag in the curved liquid–air interface is such that it touches the bottom of the groove [45,46]. The laser-modified surface demonstrates primarily the Cassie–Baxter state [41,47]; in which case, fine textured surface with low surface roughness results in air pockets occupying the texture gap. This, in turn, generates hydrophobic surface behavior. The presence of aluminum nitride in the laser-treated surface contributes to the wetting. In this case, contact angle increases since the surface energy of AlN is only  $38.3 \text{ mJ/m}^2$  while it is  $68 \text{ mJ/m}^2$  for  $\text{Al}_2\text{O}_3$  [48]. Moreover, the unmodified PEO surface demonstrates primarily the Wenzel

state, which can be attributed to the surface texture of the untreated workpiece. Although the PEO treatment results in increased roughness because of the nonuniform current density across the surface during the process, the surface texture formed exhibits randomly distributed pillars with different heights. Consequently, air trapped within the texture does not form a permanent interlayer between the workpiece surface and the water droplets. In some regions of the surface, hydrophobicity of the surface increases because of closely spaced fine pillars at the surface. However, this occurs randomly and the total area of coverage in this region is small for the unmodified surface. Nevertheless, that surface is composed of consisting of a mixture hydrophobic Cassie–Baxter and Wenzel states. The contact angle measurements reveal that the laser-modified surface demonstrates super hydrophobicity. This can be observed from Table 5, in which the contact angle data are given. The roughness factor ( $f$ )

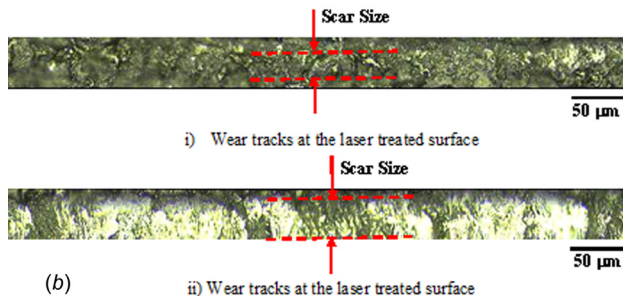
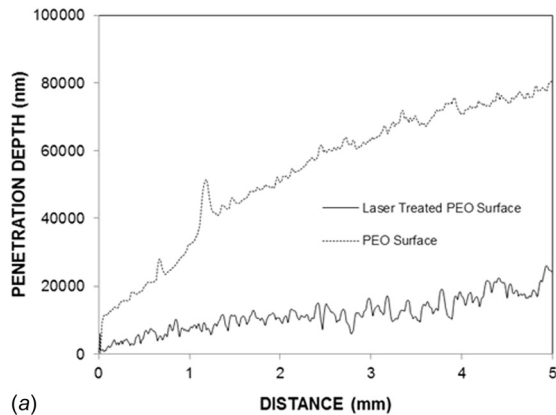


**Fig. 6** (a) Scar depth for laser treated PEO and untreated PEO surfaces and (b) wear tracks resulted during the starch tests: (i) laser-treated PEO surface and (ii) PEO surface

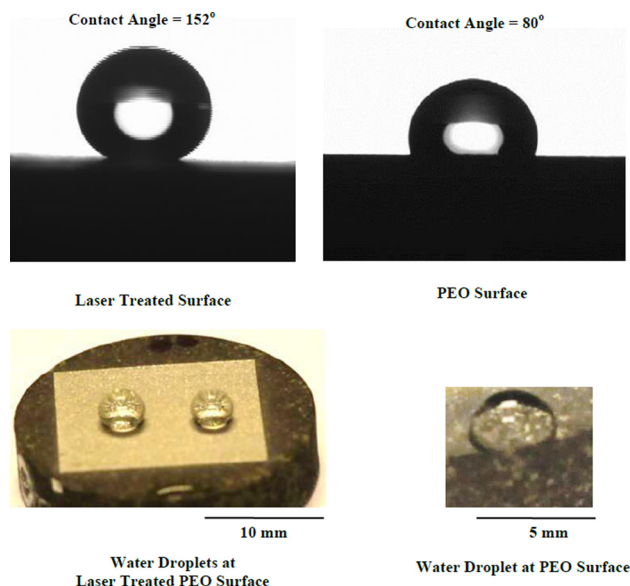


**Fig. 7** Micrographs and photographs representing the hydrophobic state of the PEO and laser-treated PEO surfaces

**Table 5** Microhardness prior to and after the laser treatment of PEO surfaces

	Hardness (HV)
Laser-treated PEO surface	1700 ( $\pm 50$ )
PEO-treated surface	1250 ( $\pm 50$ )
As received aluminum 6061 surface	105

**Table 6** Contact angles measurement results prior to and after the laser treatment of PEO surfaces

	Contact angle (deg)
Laser-treated PEO surface	151.6 ( $\pm 5$ )
PEO surface	83.4 ( $\pm 5$ )

should be within  $0 \leq f \leq 1$  for the hydrophobic surfaces, in accordance with Eq. (3). However, super hydrophobicity is only possible for  $f$  values approaching zero. Therefore,  $f$  should approach 0 for large contact angles in the Cassie–Baxter state. This situation is possible when the surface texture is composed of a mixture of microsized and nanosized dimples and pillars, which in turn gives rise to the Cassie–Baxter state, with large contact angles (Table 6).

## Conclusions

It has been shown that the texture of a plasma electrolytically oxidized surface of aluminum 6061 alloy consists of irregular distributions of dimples and pillars, which lowers the hydrophobicity at the surface. Controlled laser ablation modification results in regular texture patterns along the laser scanning tracks. The laser-treated surface consists of micropillar—and nanopillar, which reduce the wetting state of the surface significantly; in this case, the Cassie–Baxter state dominates over the surface and super hydrophobic characteristics result. The laser-treated surface is free from large asperities and cracks, despite the cooling rate being high at the surface. Heat transfer from overlapping of irradiated spots with their near neighbors suppresses the thermal strains developed along the scanning tracks. In addition, recently formed laser tracks create a self-annealing effect in the adjacent, previously formed, tracks through conduction heat transfer, while also modifying the surface cooling rate within the surface vicinity. Although high pressure nitrogen gas assistance contributes to the cooling rate at the surface, its presence also initiates the formation of nitride species, such as AlN and AlON. A dense, fine grained layer is formed at the surface, whilst a columnar structure is retained below the dense layer. The demarcation zone between the laser-treated region and base material can be clearly observed; however, a heat affected zone is not visibly due to the high thermal diffusivity of the aluminum alloy substrate. Microhardness increases in the laser modified PEO surface, which is associated with the contribution of the high cooling rate (and formation of nitride species) to the surface hardness of the laser-treated workpiece.

## Acknowledgment

The authors acknowledge the financial support of King Fahd University of Petroleum and Minerals (KFUPM) through Project No. MIT11111-11112, and King Abdulaziz City for Science and Technology (KACST) through Project No. 11-ADV2134-04 to accomplish this work.

## References

- [1] Drozdowski, K., Tofil, A., Gontarz, A., Pater, Z., and Tomczak, J., 2013, "Manufacturing Process of Plane Rim From Aluminum Alloy," *Aircr. Eng. Aerosp. Technol.*, **85**(6), pp. 487–492.
- [2] Gopi, K. R., Mohandas, K. N., Reddappa, H. N., and Ramesh, M. R., 2013, "Characterization of as Cast and Heat Treated Aluminum 6061/Zircon Sand/Graphite Particulate Hybrid Composites," *Int. J. Eng. Adv. Technol.*, **2**(5), pp. 340–344.
- [3] "Aluminium and Aluminium Alloys," [http://www.contactaliminaire.com/fileadmin/ImageFichier\\_Archive/contact\\_aliminaire/Fichiers\\_Documents/Brochure\\_JO/Note\\_2004\\_64\\_anglaise/Aluminium\\_sheet\\_1.pdf](http://www.contactaliminaire.com/fileadmin/ImageFichier_Archive/contact_aliminaire/Fichiers_Documents/Brochure_JO/Note_2004_64_anglaise/Aluminium_sheet_1.pdf)
- [4] Nie, X., Meletis, E. I., Jiang, J. C., Leyland, A., Yerokhin, A. L., and Matthews, A., 2002, "Abrasive Wear/Corrosion Properties and TEM Analysis of Al<sub>2</sub>O<sub>3</sub> Coatings Fabricated Using Plasma Electrolysis," *Surf. Coat. Technol.*, **149**(2–3), pp. 245–251.

- [5] Hussein, R. O., Nie, X., Northwood, D. O., Yerokhin, A., and Matthews, A., 2010, "Spectroscopic Study of Electrolytic Plasma and Discharging Behaviour During the Plasma Electrolytic Oxidation (PEO) Process," *J. Phys. D: Appl. Phys.*, **43**(10), pp. 105203–105216.
- [6] Yilbas, B. S., Khaled, M., Abu-Dheir, N., Aqeeli, N., and Furquan, S. Z., 2013, "Laser Texturing of Alumina Surface for Improved Hydrophobicity," *Appl. Surf. Sci.*, **286**, pp. 161–170.
- [7] Yerokhin, A. L., Nie, X., Leyland, A., Dowey, S. J., and Matthews, A., 1999, "Review: Plasma Electrolysis for Surface Engineering," *Surf. Coat. Technol.*, **122**(2–3), pp. 73–93.
- [8] Han, J. T., Xu, X. R., and Cho, K. W., 2005, "Diverse Access to Artificial Superhydrophobic Surfaces Using Block Co-polymers," *Langmuir*, **21**(15), pp. 6662–6665.
- [9] Shirtcliffe, N. J., McHale, G., Newton, M. I., Chabrol, G., and Perry, C. C., 2004, "Dual-Scale Roughness Produces Un-usually Water-Repellent Surfaces," *Adv. Mater.*, **16**(21), pp. 1929–1932.
- [10] Hwang, H. S., Lee, S. B., and Park, I., 2010, "Fabrication of Rasp-Berry-Like Superhydrophobic Hollow Silica Particles," *Mater. Lett.*, **64**(20), pp. 2159–2162.
- [11] Huang, Y. H., Wu, J. T., and Yang, S. Y., 2011, "Direct Fabricating Patterns Using Stamping Transfer Process With PDMS Mold of Hydrophobic Nanostructures on Surface of Micro Cavity," *Microelectron. Eng.*, **88**(6), pp. 849–854.
- [12] Yang, T., Tian, H., and Chen, Y., 2009, "Preparation of Superhydrophobic Silica Films With Honeycomb-Like Structure by Emulsion Method," *J. Sol-Gel Sci. Technol.*, **49**(2), pp. 243–246.
- [13] Kinoshita, H., Ogasahara, A., Fukuda, Y., and Ohmae, N., 2010, "Superhydrophobic/Superhydrophilic Micropatterning on a Carbon Nanotube Film Using a Laser Plasma-Type Hyperthermal Atom Beam Facility," *Carbon*, **48**(15), pp. 4403–4408.
- [14] Latthe, S. S., Imai, H., Ganesan, V., and Rao, A. V., 2009, "Super-Hydrophobic Silica Films by Sol-Gel Co-Precursor Method," *Appl. Surf. Sci.*, **256**(1), pp. 217–222.
- [15] Ma, M., Mao, Y., Gupta, M., Gleason, K. K., and Rutledge, G. C., 2005, "Superhydrophobic Fabrics Produced by Electrospinning and Chemical Vapor Deposition," *Macromolecules*, **38**(23), pp. 9742–9748.
- [16] Yilbas, B. S., and Bhushan, B., 2014, "Laser Treatment of Sintered Silicon Carbide Surface for Enhanced Hydrophobicity," *JOM*, **66**(1), pp. 87–94.
- [17] Choi, S. C., Kim, C. S., Jhang, K., and Shin, W., 2012, "Surface Characteristics of Aluminum 6061-T6 Subjected to Nd:YAG Pulsed-Laser Irradiation," *J. Mech. Sci. Technol.*, **26**(7), pp. 2163–2166.
- [18] Nair, R., Jiang, W., and Mohan, P., 2008, "Synthesis of Diamond-Like Carbon Coatings on Aluminum 6061 T-91 Substrates by Laser Sintering of Ultra-Nanocrystalline Diamond Powders," *Surf. Coat. Technol.*, **202**(13), pp. 2935–2944.
- [19] Xu, F., Guo, Y., Gong, S., Chen, L., and Guo, L., 2012, "Microstructure and Mechanical Properties of 6061 Aluminum Alloy by Laser Welding With Filling Wire," *Adv. Mater. Res.*, **510**, pp. 585–589.
- [20] Wang, C. D., Zhou, J. Z., Huang, S., Yang, X. D., Xu, Z. C., and Ruan, H. Y., 2011, "Study on the Improvement of Fatigue Crack Growth Performance of 6061-T6 Aluminum Alloy Subject to Laser Shot Peening," *Key Eng. Mater.*, **464**, pp. 391–394.
- [21] Gencalp Irizalp, S., Saklakoglu, N., Akman, E., and Demir, A., 2014, "Pulsed Nd:YAG Laser Shock Processing Effects on Mechanical Properties of 6061-T6 Alloy," *Opt. Laser Technol.*, **56**, pp. 273–277.
- [22] Zhang, J., Weckman, D. C., and Zhou, Y., 2008, "Effects of Temporal Pulse Shaping on Cracking Susceptibility of 6061-T6 Aluminum Nd:YAG Laser Welds," *Weld. J.*, **87**(1), pp. 18s–30s.
- [23] Katipelli, L. R., Agarwal, A., and Dahotre, N. B., 2000, "Laser Surface Engineered TiC Coating on 6061 Al Alloy: Microstructure and Wear," *Appl. Surf. Sci.*, **153**(2), pp. 65–78.
- [24] Gomez-Rosas, G., Rubio-Gonzalez, C., Ocana, J. L., Molpeceres, C., Porro, J. A., Morales, M., Casillas, F. J., Mora-Gonzalez, M., and Chi-Moreno, W., 2007, "Laser Shock Processing to Improve Residual Stresses With and Without Paint Layer on 6061-T6 Aluminum Alloy," Proceedings of the SPIE International Society for Optical Engineering Sixth Symposium Optics in Industry, Monterrey, Mexico, Paper No. 64220U.
- [25] Sanchez-Santana, U., Rubio-Gonzalez, C., Gomez-Rosas, G., Ocana, J. L., Molpeceres, C., Porro, J., and Morales, M., 2006, "Wear and Friction of 6061-T6 Aluminum Alloy Treated by Laser Shock Processing," *Wear*, **260**(7–8), pp. 847–854.
- [26] Sathyajith, S., and Kalainathan, S., 2012, "Effect of Laser Shot Peening on Precipitation Hardened Aluminum Alloy 6061-T6 Using Low Energy Laser," *Opt. Lasers Eng.*, **50**(3), pp. 345–348.
- [27] Khan, R. H. U., Yerokhin, A., Li, X., Dong, H., and Matthews, A., 2010, "Surface Characterization of DC Plasma Electrolytic Oxidation Treated 6082 Aluminum Alloy: Effect of Current Density and Electrolyte Concentration," *Surf. Coat. Technol.*, **205**(6), pp. 1679–1688.
- [28] Parfenov, E. V., Yerokhin, A. L., and Matthews, A., 2007, "Impedance Spectroscopy Characterization of PEO Process and Coatings on Aluminum," *Thin Solid Films*, **516**(2–3), pp. 428–432.
- [29] Yerokhin, A. L., Nie, X., Leyland, A., and Matthews, A., 2000, "Characterisation of Oxide Films Produced by Plasma Electrolytic Oxidation on a Ti-6Al-4V Alloy," *Surf. Coat. Technol.*, **130**(2–3), pp. 195–206.
- [30] Yilbas, B. S., Khaled, M., and Karatas, C., 2011, "Laser Re-Melting of Alumina Tile Surfaces: Corrosion Testing in Aqueous Solution," *Corros. Eng. Sci. Technol.*, **46**(4), pp. 477–480.
- [31] Yilbas, B. S., Akhtar, S., and Karatas, C., 2011, "Laser Gas Assisted Melting of Pre-Prepared Alumina Surface Including TiC Particles at Surface," *Surf. Eng.*, **27**(6), pp. 470–476.
- [32] Yilbas, B. S., Al-Aqeeli, N., and Karatas, C., 2012, "Laser Control Melting of Alumina Surfaces With Presence of B<sub>4</sub>C Particles," *J. Alloys Compd.*, **539**, pp. 12–16.
- [33] Bityukov, V. K., and Petrov, V. A., 2013, "Absorption Coefficient of Molten Aluminum Oxide in Semitransparent Spectral Range," *Appl. Phys. Res.*, **5**(1), pp. 51–71.
- [34] Hapke, B., 1995, *Theory of Reflectance and Emittance Spectroscopy*, Cambridge University, Cambridge, UK.
- [35] Yilbas, B. S., Danisman, K., and Yilbas, Z., 1991, "Measurement of Temperature-Dependent Reflectivity of Cu and Al in the Range 30–1000 °C," *Meas. Sci. Technol.*, **2**(7), pp. 668–674.
- [36] Huang, Z., Cho, S., Jiang, D., and Tan, S., 1999, "Surface Nitridation of Al<sub>2</sub>O<sub>3</sub> Based Composite by N<sub>2</sub>-HIP Post-Treatment," *J. Mater. Sci.*, **34**(9), pp. 2023–2027.
- [37] Yilbas, B. S., Akhtar, S. S., and Karatas, C., 2011, "Laser Carbonitriding of Alumina Surface," *Opt. Lasers Eng.*, **49**(3), pp. 341–350.
- [38] Yilbas, B. S., Karatas, C., Arif, A. F. M., and Abdul Aleem, B. J., 2009, "Laser Gas Assisted Nitriding of Alumina Surfaces," *Surf. Eng.*, **25**(3), pp. 235–240.
- [39] Neumann, A. W., and Good, R. J., 1979, *Surface and Colloid Science*, Vol. II, R. J. Good and R. R. Stromberg, eds., Plenum Publishing, New York.
- [40] Wenzel, R. N., 1936, "Resistance of Solid Surfaces to Wetting by Water," *Ind. Eng. Chem.*, **28**(8), pp. 988–994.
- [41] Cassie, A. B. D., and Baxter, S., 1944, "Wettability of Porous Surfaces," *Trans. Faraday Soc.*, **40**, pp. 546–551.
- [42] Anand, S., Paxson, A. T., Dhiman, R., Smith, J. D., and Varanasi, K. K., 2012, "Enhanced Condensation on Lubricant-Impregnated Nanotextured Surfaces," *ACS Nano*, **6**(11), pp. 10122–10129.
- [43] Latthe, S. S., Gurav, A. B., Maruti, C. S., and Vhatkar, R. S., 2012, "Recent Progress in Preparation of Superhydrophobic Surfaces: A Review," *J. Surf. Eng. Mater. Adv. Technol.*, **2**, pp. 76–94.
- [44] Kwon, H.-W., Paxson, A. T., Varanasi, K. K., and Patankar, N. A., 2011, "Rapid Deceleration-Driven Wetting Transition During Pendant Drop Deposition on Superhydrophobic Surfaces," *Phys. Rev. Lett.*, **106**(3), p. 036102.
- [45] Jung, Y. C., and Bhushan, B., 2007, "Wetting Transition of Water Droplets on Superhydrophobic Patterned Surfaces," *Scr. Mater.*, **57**(12), pp. 1057–1060.
- [46] Bhushan, B., Jung, Y. C., and Koch, K., 2009, "Self-Cleaning Efficiency of Artificial Superhydrophobic Surfaces," *Langmuir*, **25**(5), pp. 3240–3248.
- [47] He, S., Zheng, M., Yao, L., Yuan, X., Li, M., Ma, L., and Shen, W., 2010, "Preparation and Properties of ZnO Nanostructures with Electrochemical Anodization Method," *Appl. Surf. Sci.*, **256**(8), pp. 2557–2562.
- [48] Zan, H.-W., Yen, K.-H., Liu, P.-K., Ku, K.-H., Chen, C.-H., and Hwang, J., 2007, "Low-Voltage Organic Thin Film Transistors With Hydrophobic Aluminum Nitride Film as Gate Insulator," *Org. Electron.*, **8**, pp. 450–454.